

Chemical Reaction Neural Networks for Fitting Accelerated Rate Calorimetry Data

Saakaar Bhatnagar^{a†}
 sbhatnagar@altair.com

Andrew Comerford^a
 acomerford@altair.com

Zelu Xu^a
 zxu@altair.com

Davide Berti Polato^b
 davide.bertipolato@beond.net

Araz Banaeizadeh^a
 araz@altair.com

Alessandro Ferraris^b
 alessandro.ferraris@beond.net

^aAltair Engineering Inc., 640 W. California Ave, Sunnyvale, CA, USA

^bBeonD Srl - Corso Castelfidardo, 30A, 10129 Torino, Italy

Keywords: Thermal Runaway, Accelerated Rate Calorimetry (ARC), Artificial Intelligence (AI), Chemical Reaction Neural Networks (CRNN), Neural ODE

Abstract

As the demand for lithium-ion batteries rapidly increases there is a need to design these cells in a safe manner to mitigate thermal runaway. Thermal runaway in batteries leads to an uncontrollable temperature rise and potentially fires, which is a major safety concern. Typically, when modelling the chemical kinetics of thermal runaway calorimetry data (e.g. Accelerated Rate Calorimetry (ARC)) is needed to determine the temperature-driven decomposition kinetics.

Conventional methods of fitting Arrhenius Ordinary Differential Equation (ODE) thermal runaway models to Accelerated Rate Calorimetry (ARC) data make several assumptions that reduce the fidelity and generalizability of the obtained model. In this paper, Chemical Reaction Neural Networks (CRNNs) are trained to fit the kinetic parameters of N-equation Arrhenius ODEs to ARC data obtained from a Molicle 21700 P45B. The models are found to be better approximations of the experimental data. The flexibility of the method is demonstrated by experimenting with two-equation and four-equation models. Thermal runaway simulations are conducted in 3D using the obtained kinetic parameters, showing the applicability of the obtained thermal runaway models to large-scale simulations.

1 Introduction

Thermal runaway in battery packs is a major safety concern for commercial applications such as electric vehicles, potentially leading to catastrophic outcomes like battery pack fires. This phenomenon occurs due to thermal abuse conditions that lead to exothermic degradation reactions of battery components, such as anode decomposition, cathode conversion, SEI decomposition, and electrolyte breakdown[1, 2]. Typical thermal abuse failure modes include, but are not limited to, physical damage, internal short circuits, overcharging, or overheating (e.g., extreme temperature exposure)[1]. The heat released under such conditions, when a cell or group of cells fails, can lead to a chain reaction where adjacent cells enter a self-heating state and undergo thermal runaway[3]. This propagation can consume an entire battery module or pack. These safety concerns are even more pressing in today's electrification environment, particularly as the industry moves towards higher power and energy density cells[1, 4]. To address these concerns, cell and pack manufacturers must adhere to strict safety protocols to avoid catastrophic outcomes. Simulation-driven design offers a platform to optimize designs and aid in the prevention and mitigation of thermal runaway. For example, thermal analysis of novel heat shield materials can be conducted efficiently to understand their effectiveness at mitigating propagation.

[†]Corresponding Author

Typically, when modeling thermal runaway, chemical decomposition kinetics are represented by multiple Arrhenius Ordinary Differential Equations (ODEs)[2, 5, 6]. These reaction rates, combined with the reaction enthalpy, allow for the prediction of chemical heat generation under abuse scenarios. For each of the Arrhenius ODEs, the kinetic parameters and heat of reaction must be determined. In the literature, a popular model is that proposed by Hatchard et al. [5]. This model utilized calorimetry-derived data to model thermal runaway in an 18650 Lithium Cobalt Oxide (LCO) cell for the anode, cathode, and SEI decomposition reactions. The model utilized a lumped approach, that is treating the jellyroll as a single temperature, and demonstrated excellent agreement with experimental oven tests. This model has been the basis of a number of subsequent models and has been extended to simulate other cell types, 3D domains (i.e. not lumped), additional decomposition reactions (e.g., electrolyte breakdown and short circuit events), and different cathode chemistries[6–10]. In addition to these Hatchard-derived models, parameter estimation for the generic Arrhenius ODE have been proposed in the literature. The model by Shelke et al. [11], which is similar to [5] and [6], but with the addition of a mix term to match the experimental accelerated rate calorimetry (ARC) data, is one example. Ping et al. [12] demonstrated a five-stage model also based on ARC data. The kinetic and reaction heat parameters were determined through a combination of parameter fitting and literature data. More details regarding this method are provided later. Feng et al. [13] proposed an elaborate mathematical model based on literature (e.g. [5]) and some novel formulations, demonstrating excellent agreement with the ARC experimental data. Their model utilized parameters from the literature and adjusted the parameters to fit experimental data; limited details of the fitting methods were provided. Chen et al. [14] introduced an ARC-derived two-stage model. The advantage of this model is it requires fewer parameters than the four-stage NREL model. Their approach demonstrated good agreement with the ARC experimental data. In general, the models currently in literature can intricately model the physics of thermal runaway, but parameter identification often relies on literature data or laborious and not necessarily robust identification methods.

Parameter estimation for thermal runaway modelling remains a major challenge and typically relies on calorimetry data to measure chemical heat release. In literature, there are several types of calorimetry data used, each with their own advantages and disadvantages. Some examples include: Accelerated Rate Calorimetry (ARC)[11, 13–17]; Fractional Thermal Runaway Calorimetry (FTRC) developed by NASA [18]; and Differential Scanning Calorimetry (DSC) [2, 19, 20]. FTRC can accurately measure heat generation and gas release during thermal runaway, offering the advantage of shorter experimental time frames compared to other calorimetry-based approaches. To the authors' knowledge, no fitting has been done on this data yet, but it represents a promising method. DSC is a thermal analysis technique that measures heat flow into or out of a sample (e.g. cathode material) as it undergoes a controlled temperature ramp. This heat flow can be used to characterize the heat generation of individual battery components, separately. Finally, ARC is one of the most common ways to characterize battery thermal runaway response for a single cell. In this experiment, the intact cell is first placed inside a thermally isolated cell holder in a sealed calorimeter chamber. The test initiates in a heat-wait-seek mode, where a heater heats the calorimeter incrementally, then pauses to allow thermal transients to decay and equilibrium conditions to be reached. If any increase in temperature rate surpasses a preset threshold value (indicating exothermic reactions), the calorimeter switches to exotherm mode. In this mode, the calorimeter tracks the temperature rise and maintains zero temperature differential between the cell surface and the calorimeter walls, ensuring adiabatic conditions. The final phase involves either full thermal runaway and subsequent cooling or simply cooling if the temperature rate falls below the preset threshold value.

Typically in the literature, the most common method for determining reaction heat and kinetic parameters from ARC calorimeter-based data involves introducing temperature stages and linearizing the governing Arrhenius kinetic ODE within these stages[12, 14]. Parameters are then determined using least squares fitting. Dividing the data into more stages generally leads to a better representation of the underlying data. These types of thermal runaway models can be considered cell-based models as they do not directly elucidate the individual reaction kinetics of the electrodes[21]. Alternative models that provide more detailed reaction kinetic information, are the DSC component-based models (e.g. [19, 22]). Unfortunately, for the cell-based models, the numerous approximations made during the linearization process reduce the fidelity of the model and often fail to accurately represent the

underlying data (see section 3.2). Some of these inaccuracies can be alleviated through manual tuning, ultimately yielding a reasonable representation of the original data and the physical phenomena can be obtained, albeit through a laborious process.

Chemical Reaction Neural Networks (CRNNs) have been proposed to discover reaction coefficients, parameters and pathways in systems governed by the Arrhenius equations [23]. In CRNNs, the differential equation

$$\frac{dc}{dt} = f(\mathbf{c}, \boldsymbol{\theta}, t), \quad (1)$$

is integrated in a fully differentiable manner w.r.t $\boldsymbol{\theta}$, similar to Neural ODEs [24], where f is the neural network formulated using the system of ODEs governing the chemical reactions modelled, $\boldsymbol{\theta}$ are time-independent parameters to be learnt using stochastic gradient descent using a loss metric, and \mathbf{c} represents the time-dependent system state.

Puliyanda et al. [25] used CRNNs to obtain chemical kinetic models from noisy spectroscopic data, achieving significant performance improvements over least squares regression. Kircher et al. [26] proposed the Global Reaction Neural Network (GRNN) architecture, embedding thermodynamic and stoichiometric prior knowledge into the network architecture, which autonomously learned kinetic models directly from noisy reactor data. Koenig et al. [22] used CRNNs to learn the thermal decomposition models of Nickel-Cobalt-Manganese (NMC) cathodes using DSC data, obtaining more physically consistent fits by avoiding empirical assumptions made when fitting using the Kissinger method[27]. These studies demonstrated that, since the learned parameters are constrained to obey the governing ODEs, the physics-informed nature of the CRNN method outperformed other data-driven methods in terms of better accuracy and lower data requirements. Additionally, the resulting models are physically interpretable in the form of the governing ODEs.

This work proposes a novel method to obtain accurate fits for Arrhenius equation-based thermal runaway models from experimental Accelerated Rate Calorimetry (ARC) data. CRNNs are utilized to learn the required parameters. A staging and linearization-based fitting method is demonstrated on the data, showing its shortcomings in creating accurate models. The obtained parameters are then tuned via training a CRNN, resulting in learned models that better represent the data. The experiment is conducted on two and four-stage models, showing the flexibility of the method. The tuned parameters are tested in 3D simulations of ARC and oven tests, demonstrating improved workflow and performance compared with more traditional methods cited in the literature.

2 Experimental Setup

The battery cell under investigation was a Molicle 21700 P45B with a mass of 0.066kg and a capacity of 4.5Ah. The sample cell was inserted into a holder within the ARC reactor. The cell was preconditioned by gradually heating it to a controlled temperature of 50°C. These conditions were allowed to equilibrate to ensure a uniform baseline temperature. To investigate thermal runaway, a Heat-Wait-Seek (HWS) testing protocol was employed. Initially, the cell underwent a temperature ramp exceeding 0.02°C/min to bring it close to the onset of self-heating. Once stabilized at this temperature, the ARC initiated the HWS protocol. During this protocol, the sample was heated in increments of 5 °C and then allowed to equilibrate (“wait”) for over 40 minutes. Adiabatic conditions were maintained by adjusting the chamber temperature to match that of the cell. Subsequently, the calorimeter entered a “seek” mode for 10 minutes to detect any exothermic activity: If any signs of self-heating (e.g., a sustained temperature rise of 0.02 °C/min), the ARC transitioned to exotherm mode, otherwise the heat-wait-seek cycle was repeated. In exotherm mode, the ARC tracked the temperature rise due to exothermic reactions and endeavored to maintain adiabatic conditions by dynamically adjusting the chamber temperature and provide detailed thermal behavior such as cell (top, middle and bottom) as well as ambient temperature. The setup of the cell within the chamber and the location of thermocouples on the cell surface are shown in Figures (1a)-(1c).

The collected ARC data is used to determine the heat rate (in °C/min) versus temperature (in °C), as well as temperature versus time. Figures (1d) and (1e) show the collected data for heat rate versus temperature and temperature versus time, respectively.

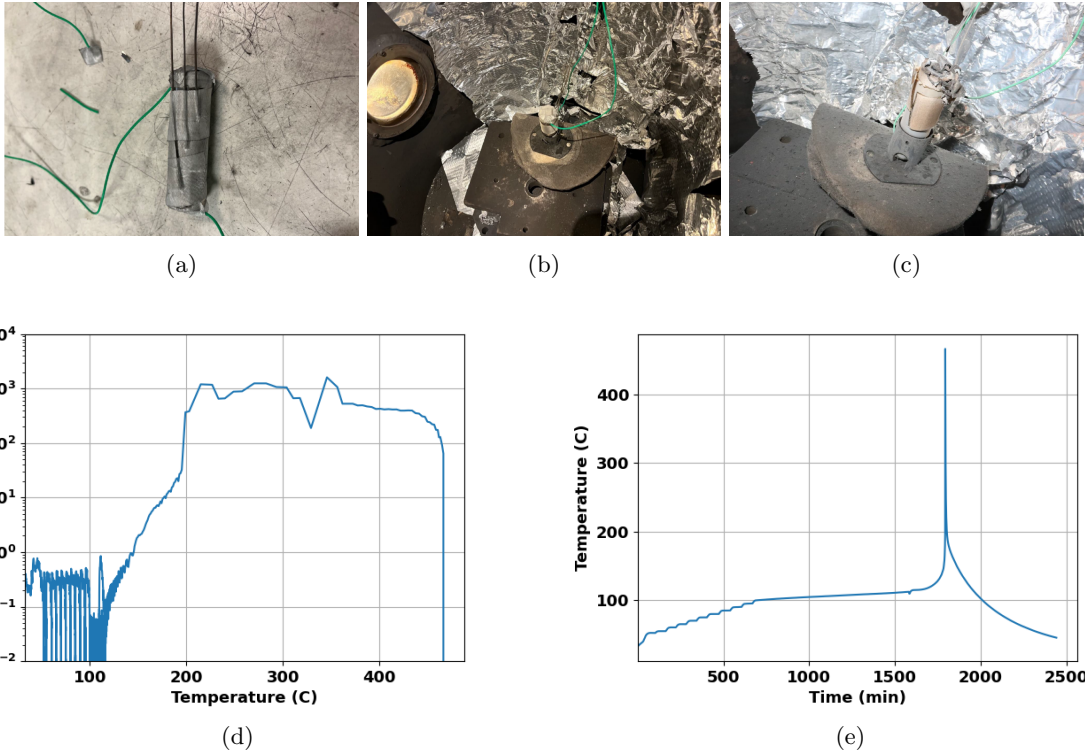


Figure 1: ARC experimental testing (a) Location of thermocouples on the cell surface to measure cell temperature (b) Cell in holder inside ARC chamber (c) Burnt out cell post ARC test (d) Heat rate versus temperature (e) Temperature evolution with time

3 Methods and Models

3.1 TR ODE System

The thermal runaway modelling equations in this work take the form of an Arrhenius reaction equation to model the decomposition kinetics and are given by,

$$\frac{dc_i}{dt} = f_i(c_i) A_i e^{\frac{-E_{a,i}}{k_b T}}, \quad i=1,2,\dots,N \quad (2)$$

$$f_i(c_i) = c_i^{n_i} (1 - c_i)^{m_i}, \quad (3)$$

where c_i is the normalized reactant concentration, A_i is the frequency factor, $E_{a,i}$ is the activation energy, k_b is the Boltzmann constant, T is the temperature, and N refers to the number of stages in the model. m_i and n_i are reaction orders from the rate law. The reaction orders determine whether the reaction is n th order (when $m_i = 0$) or an auto-catalytic type i.e. the reaction increases as the product is generated ($m_i > 0$) [28, 29].

The heat Q_i from each exothermic stage decomposition can be calculated using

$$\dot{Q}_i = h_i \frac{dc_i}{dt}, \quad (4)$$

where h_i is the reaction enthalpy. The temperature update of the cell due to the thermal runaway can then be computed using

$$m_{cell} c_p \frac{dT}{dt} = \sum_{i=1}^N \dot{Q}_i + \dot{Q}_{diss}, \quad (5)$$

where m_{cell} and c_p represent the mass and specific heat of the cell respectively, and \dot{Q}_{diss} is the dissipative heat flux due to natural convection and radiation. This term is modelled as

$$\dot{Q}_{diss} = A_{cell}[h_{conv}(T_{\infty} - T) + \epsilon\sigma(T_{\infty}^4 - T^4)], \quad (6)$$

where A_{cell} refers to the area of the cell, h_{conv} is the convective heat transfer coefficient [30], $\epsilon = 0.8$, σ is the Stefan-Boltzmann constant, and T_{∞} is the far field temperature.

A good model representing the the thermal runaway process is achieved by obtaining the values of the following kinetic and reaction heat parameters,

$$\theta_i = [A, E_a, h, m, n]_i, \forall i=1,2..N, \quad (7)$$

such that the temperature and heat rate profiles (shown in Figure 2) predicted by integrating the model are a close match to the experimental ARC data.

3.2 Linearized Arrhenius kinetics

The most common method for fitting the unknown parameters described by Equation 7 to ARC data involves staging and linearizing the governing equations of the model. The number of stages, N , depends on the specific model. For example, Chen et al. [14] used a two-stage model, whereas Sun et al. [31] and Ping et al. [12] used four and five-stage models, respectively, to describe the thermal runaway process.

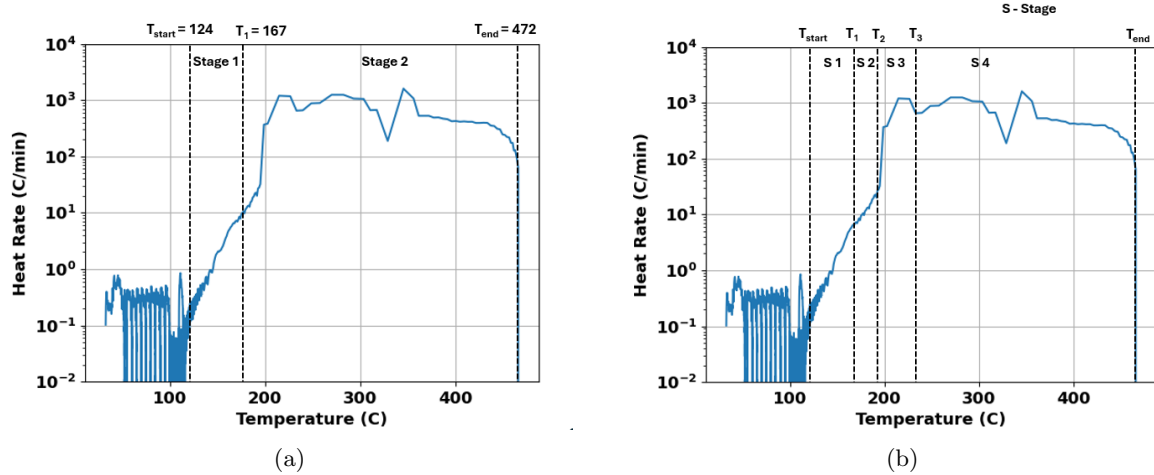


Figure 2: Division of data into stages, showing the start and end temperature for each stage (2a) A two-stage fit (2b) A four-stage fit

Figure (2a) shows the division of ARC experimental data into two stages, and Figure (2b) shows a four-stage division. In this section, linearization is demonstrated for a two-stage fit. Stage one starts at T_{start} and ends at T_1 , and Stage two starts at T_1 and ends at T_{end} . Every equation of the model is assigned a stage. The enthalpy of stage i is approximated by

$$h_i = mc_p(T_i^{end} - T_i^{start}). \quad (8)$$

Equations 2 - 5 are rewritten, through a series of simplifying assumptions described in [14, 31] as

$$\ln \left[\frac{dT}{dt} \right] = \ln[A_i(T_i^{end} - T_i^{start})] - \frac{E_{a,i}}{RT}. \quad (9)$$

Utilizing the staged experimental data, the slope and intercept of the $\ln(\frac{dT}{dt})$ v/s $\frac{1}{T}$ plot return the value of $E_{a,i}$ and A_i respectively.

The linearization method, although straightforward to implement, relies on a set of assumptions that limits its applicability. For example, it typically assumes a linear decrease in reactant concentration as a function of temperature [31]. However, in practice, integrating the models usually reveals a nonlinear dependency of c_i on T [14]. Furthermore, the reaction orders (m_i, n_i) are often adopted from previous studies and, therefore, may not fit the current dataset, resulting in a sub-optimal fit.

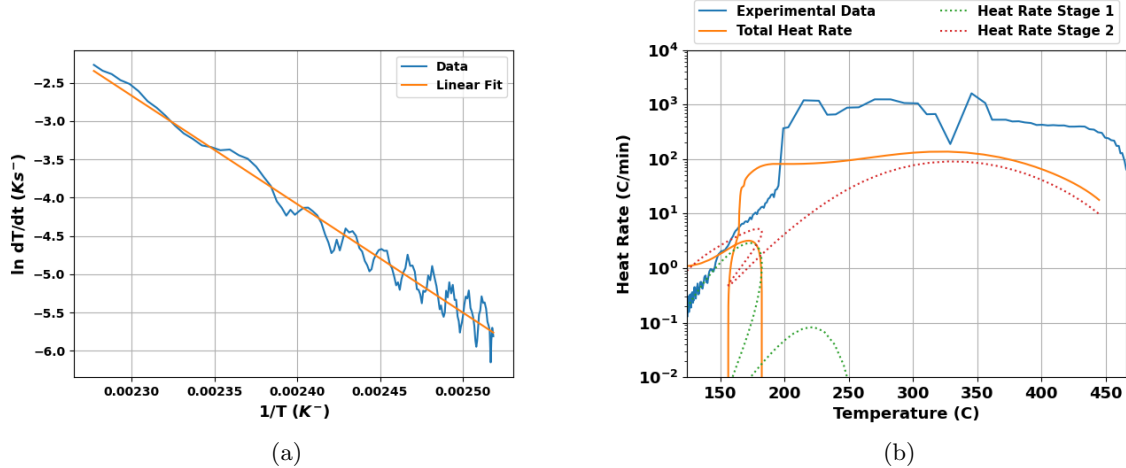


Figure 3: (a) Linear fit of stage 1 (b) Two-stage fit from linearization method

Finally, the enthalpy condition in Equation 8 assumes complete reactant concentration conversion at the end temperature of the stage, which may not hold true upon integrating the ODE models.

These assumptions can result in poor fits to experimental ARC data. Figure (3a) shows the linear fit for stage one, which appears to represent the data well. However, Figure (3b) illustrates the resultant heat rate of the fit. Unfortunately, the fit does not effectively represent the experimental data.

3.3 CRNN for ARC data fitting

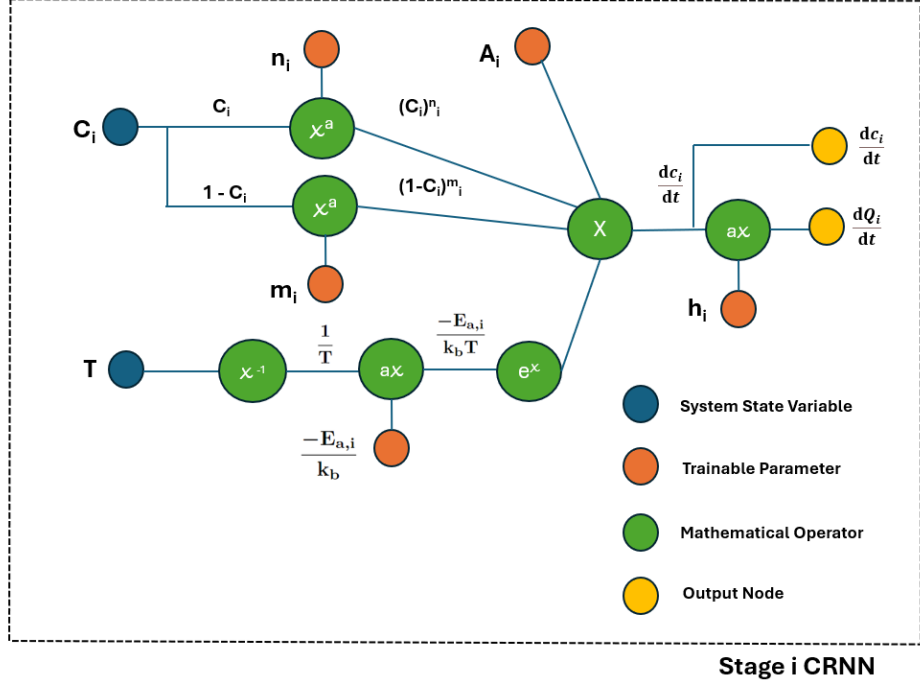
In a CRNN, the parameters to be fitted are treated as trainable variables. Instead of linearizing the governing ODEs, and obtaining the parameters by minimizing a least squares error, the governing ODEs are directly learned using the data, with parameter updates made iteratively via a gradient-based approach. An advantage of this method is that no simplifying assumptions are made on the ODE system, leading to no loss of accuracy or generality during the fitting process. Figure (4a) shows the setup of a CRNN subnetwork for stage i , where each stage has a corresponding subnetwork with unique trainable parameters. The orange nodes denote trainable parameters (obtained via gradient-based optimization), and the blue nodes denote state variables, the time histories of which are obtained via ODE integration. The output of a subnetwork is the concentration reaction rate $\frac{dc_i}{dt}$ and the rate of heat generated \dot{Q}_i by stage. Figure (4b) shows how each subnetwork is assimilated into the overall training loop. The resultant system of ODEs is integrated via a differentiable ODE integrator, and the system state $[c_1(t), c_2(t), \dots, c_N(t), T]$ is used to compute the loss \mathbf{L} relative to the experimental data. Reverse-mode automatic differentiation [32] is leveraged to compute $\frac{\partial \mathbf{L}}{\partial \theta_i}$, which is then used to update the values of θ_i via gradient descent.

In this work, the trainable parameters θ_i in the CRNN are initialized using the linearization method (Section 3.2). This improved initial guess, over random initialization, accelerates the optimization process. The loss function used to measure the difference between the predicted solution is the L_2 norm of temperature history:

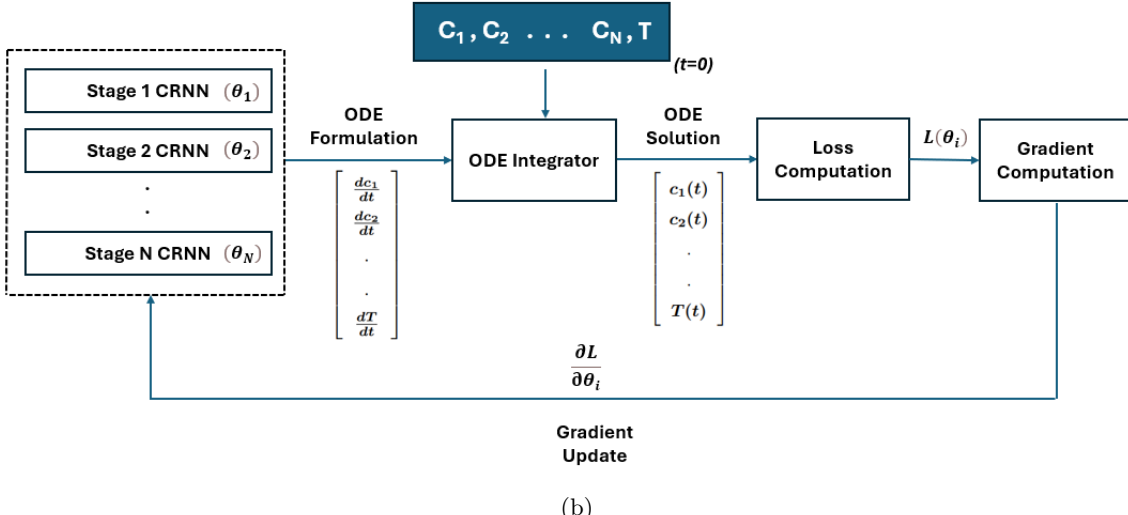
$$Loss = \frac{\sum_{j=1}^{N_{ts}} (T_j^{pred} - T_j^{truth})^2}{N_{ts}}, \quad (10)$$

where N_{ts} is the number of timesteps.

The fully differentiable computational training loop was set up using the JAX [33] automatic differentiation framework. The differentiable ODE solver library Diffraex [34], based on JAX, was used to solve the CRNN ODE system. Kvaerno's 5th order method [35] is employed for the numerical stiff ODE solve, and the Adam [36] optimizer is utilized to minimize the loss. For all results shown, the optimization is done for 10,000 steps with a scheduled learning rate, starting at 10^{-3} and decreasing by a factor of 0.9 every 300 steps.



(a)



(b)

Figure 4: (a) CRNN subnetwork diagram for a single stage. The orange nodes denote trainable variables updated via gradient-based optimization, given by $\theta_i = [A_i, E_{a,i}, h_i, m_i, n_i]$. The blue nodes represent system state variables integrated via a differentiable ODE integrator. (b) Computation graph for a single CRNN training step. Every CRNN subnetwork (Figure 4a) is assimilated to set up the ODE system, which is embedded into the training loop to learn θ_i .

4 Results and Discussion

A CRNN is used to fit the ARC data shown in Figure 2. The data is divided into N stages, every stage is linearized and a fit for the kinetic parameters θ_i is obtained $\forall i = 1, \dots, N$. The obtained parameters are used to initialize the CRNN and are improved via optimizing the loss of the CRNN (given by Equation 10) iteratively. The fitting process is demonstrated for $N=2$ and $N=4$, showing the flexibility of the proposed method. The model obtained from the four-stage fit is used in a 3D simulation of ARC and oven tests, to demonstrate the portability of the resulting thermal runaway models to accurate

Name	Mass (Kg)	Area (m^2)	Specific Heat ($JKg^{-1}K^{-1}$)
Value	0.066	4.618E-3	859

Table 1: Physical properties of the cell

3D simulations.

Table 1 lists the values of the cell properties. The initial values for reaction orders m_i, n_i are chosen based on commonly observed values in literature.

4.1 Two-stage model

A two-stage model of the ARC data takes the form:

$$\frac{dc_1}{dt} = c_1 A_1 e^{(\frac{-E_{a,1}}{RT})}, \quad (11)$$

$$\frac{dc_2}{dt} = (1 - c_2)^{m_2} A_2 e^{(\frac{-E_{a,2}}{RT})}, \quad (12)$$

$$mc_p \frac{dT}{dt} = \sum_{i=1}^2 h_i \frac{dc_i}{dt}, \quad (13)$$

with Equations 11 and 12 being particular instances of Equation 2. This model lumps the overall heat generation process into two terms and can still be motivated by the chemical kinetics of the decomposition reactions. For example, during stage one, two dominant decomposition exothermic reactions contribute to heat generation: the decomposition of the SEI and the reaction of intercalated lithium at the anode with electrolyte. In the second stage, which is the dominant source of heat, the following processes can be observed: electrolyte decomposition; cathode material decomposition and release of oxygen; the reaction of released oxygen with the electrolyte; and potentially an internal short circuit (ISC) due to separator melting. Examples of the different reaction processes can be found in the literature, e.g. Kim et al. [6], Coman et al. [8], Feng et al. [13], Chen et al. [14] among others.

The description of the staging and linearization is identical to Section 3.2 and is omitted here for brevity. The temperatures used for the staging, as shown in Figure (2), were $T_{start} = 124^\circ C$, $T_1 = 167^\circ C$, and $T_{end} = 472^\circ C$. Figure (5) shows the integrated solution for parameters initially returned from the linear fit (Figs. (5a),(5c)), and for parameters after training a CRNN (Figs. (5b), (5d)). Figure (5a) shows the temperature increase with time compared to the experimental data, and it is observed that there is a significant difference in the profile of temperature evolution. An overprediction of temperature is observed until the system is close to thermal runaway, where it turns to an underprediction and the thermal runaway time is not correctly predicted. Figure (5c) shows the heat rate plotted against temperature, and a significant deviation of the prediction is observed with respect to the experimental data.

After CRNN training, where the linear fit results are used to initialize the CRNN parameters, Figures (5b) and (5d) show much better adherence to the experimental data. The temperature leading up to and during thermal runaway is in better agreement with the experimental data, and the thermal runaway time and peak temperature is better predicted. The heat rate prediction is closer to experimental observation as well. The "linear" part of the heat rate increase is better approximated, and the region of large heat rate is approximated by the model more closely, leading to a better fit overall.

Table 2 shows each parameter fitted, for each stage, before and after CRNN training. The improved parameters are listed in bold font.

4.2 Four-stage model

A four-stage model fitted to the ARC data gives more flexibility and will yield a better approximation of the heat rate data. The model takes the form:

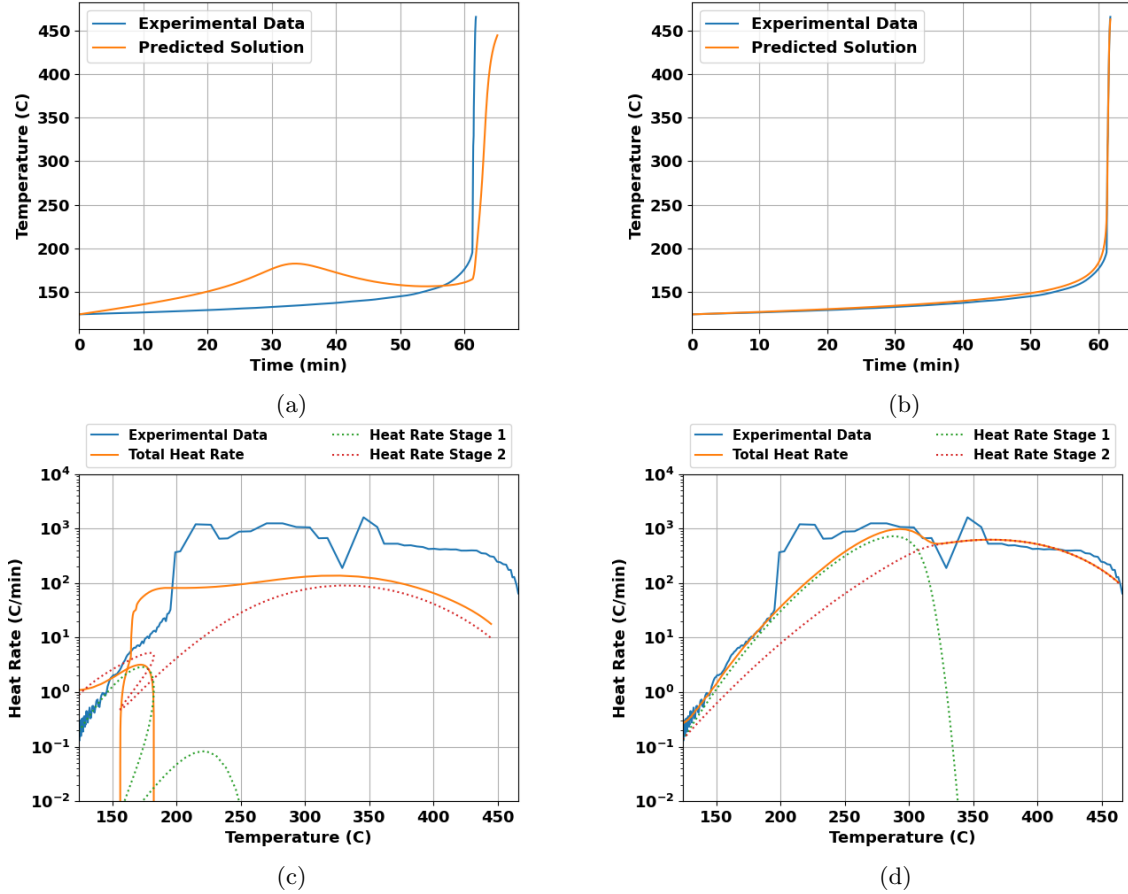


Figure 5: (a) Temperature evolution from linear fitting (b) Temperature evolution after CRNN training (c) Heat rate evolution from linear fitting (d) Heat rate evolution after CRNN training

Stage No.	Fit Method	I.C ($c_{i,0}$)	$A_i(s^-)$	$E_{a,i}$ (J)	h_i (J)	m_i	n_i
Stage 1	Linear	1.0	2.1755E11	1.9530E- 19	2434	0	1
	CRNN	1.0	1.723E11	2.027E-19	8336	0	1
Stage 2	Linear	0.04	2.927E7	1.474E-19	16963	5	0
	CRNN	0.04	1.994E7	1.554E-19	15970	4.62	0

Table 2: Parameter values for the two-stage model. For each stage, the top row lists the parameters obtained from linearization, and the boldfaced values in the bottom row are the parameters obtained after CRNN training.

$$\frac{dc_1}{dt} = c_1 A_1 e^{(\frac{-E_{a,1}}{RT})}, \quad (14)$$

$$\frac{dc_2}{dt} = c_2 A_2 e^{(\frac{-E_{a,2}}{RT})}, \quad (15)$$

$$\frac{dc_3}{dt} = c_3^{n_3} (1 - c_3)^{m_3} A_3 e^{(\frac{-E_{a,3}}{RT})}, \quad (16)$$

$$\frac{dc_4}{dt} = c_4 (1 - c_4)^{m_4} A_4 e^{(\frac{-E_{a,4}}{RT})}, \quad (17)$$

$$mc_p \frac{dT}{dt} = \sum_{i=1}^4 h_i \frac{dc_i}{dt}. \quad (18)$$

The reaction kinetics in this model are more representative of the physical processes occurring during thermal runaway. Figure (2b) graphically shows the division of stages, which were subsequently linearized and the parameters θ_i obtained. Table 3 details the values of the temperatures at which the stages are divided.

T_{start}	T_1	T_2	T_3	T_{end}
124	161	191	257	472

Table 3: Staging temperatures for the four-stage fit depicted in Figure (2b), all values in $^{\circ}\text{C}$

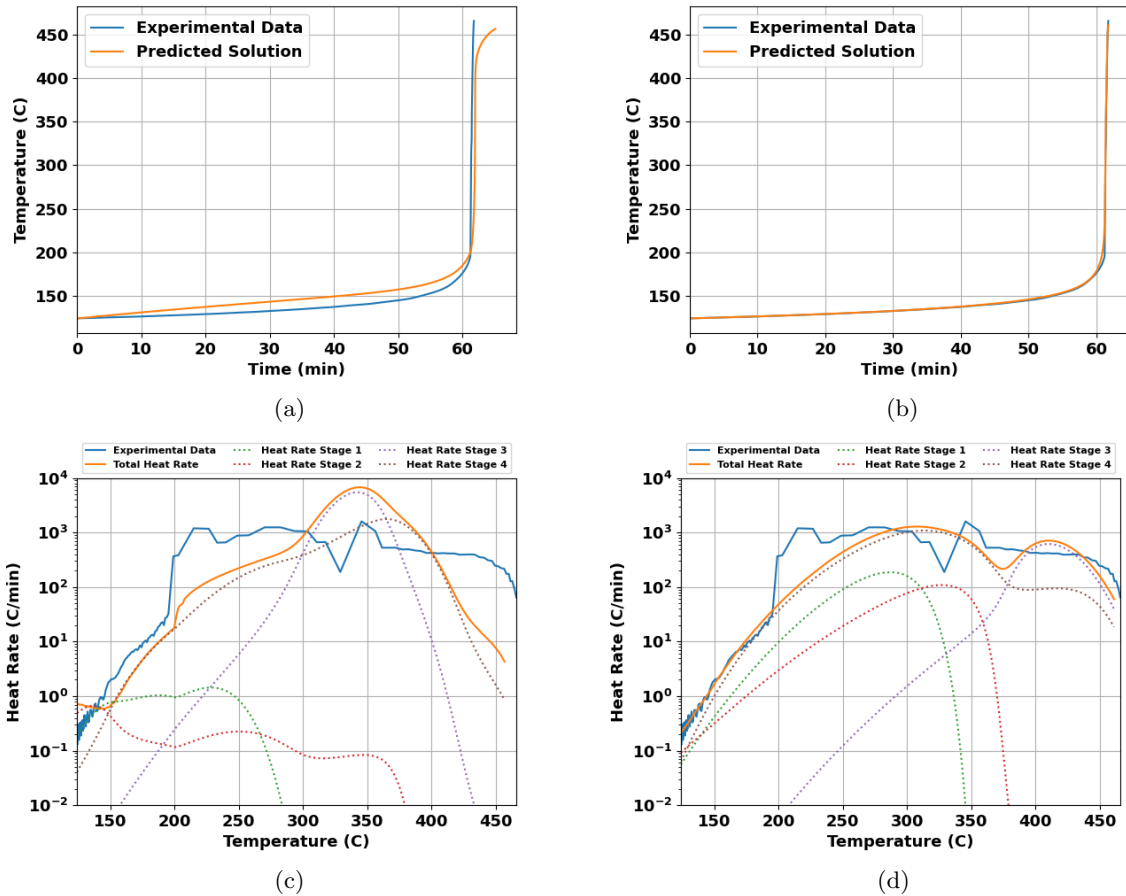


Figure 6: (a) Temperature evolution from linear fitting (b) Temperature evolution after CRNN training (c) Heat rate evolution from linear fitting (d) Heat rate evolution after CRNN training

Similar to the results in Section 4.1, Figure (6a) shows that the temperature tracked higher relative to the experimental data and was generally a poor representation of the experimental data. Figure (6c) shows the corresponding heat rate; significant differences were observed from the experimental data.

The parameters obtained for the linear fit were used to initialize the CRNN training process. Figure (6b) shows the temperature evolution with time. The fit qualitatively shows good agreement with the experimental data, both in the self-heating phase and during the rapid temperature rise of thermal runaway. Additionally, the fitted data shows a better prediction of the time the system went

Stage No.	Fit Method	I.C ($c_{i,0}$)	$A_i(s^-)$	$E_{a,i}$ (J)	h_i (J)	m_i	n_i
Stage 1	Linear	1.0	1.3859E11	1.9209E-19	2150	0	1
	CRNN	1.0	9.480E10	1.969E-19	2212	0	1
Stage 2	Linear	1.0	4.620E7	1.4174E-19	1700	0	1
	CRNN	1.0	2.550E7	1.462E-19	1330	0	1
Stage 3	Linear	0.04	2.371E11	1.941E-19	3685	2	2
	CRNN	0.04	3.936E10	2.072E-19	5696	6.34	1.94
Stage 4	Linear	0.04	2.371E11*	1.941E-19 *	11861	5	1
	CRNN	0.04	2.831E11	1.931E-19	12980	4.61	1

Table 4: Parameters fit for the four-stage model. For each stage, the top row is the parameters obtained from linearization, and the boldfaced values in the bottom row are obtained after CRNN training. The initial values for A_i and $E_{a,i}$ for stage 4, denoted by *, were initialized to be the same as the initial values for stage 3

into thermal runaway and the overall peak temperature. As an additional observation, the obtained temperature profile for the four-stage fit (Figure 6b) adheres better to the experimental data compared with the two-stage fit (Figure 5b). This is attributed to the four stages giving the model more ability to accurately represent the data.

Comparing Figure (6c) and (6d), the linear part of the rate curve, corresponding to the slow increase in temperature, is once again better approximated after the CRNN training. The sudden increase in heat rate occurring around 200 °C is captured slightly more accurately when compared to the two-stage model, leading to a better prediction of the time when thermal runaway occurs.

Table 4 shows the parameters for each stage, before and after CRNN optimization. The initial values of A_i and $E_{a,i}$ for stage 4 are set as the initial values for stage 3. This was done because the parameters obtained via linearization for stage 4 were too poor to use as initial conditions for the CRNN training.

The results obtained in Sections 4.1 and 4.2 demonstrate the improvement in parameters achieved through linearization using the CRNN method. The works by Chen et al. [14] and Ping et al. [12] utilize the linearization method, which, as shown in previous sections, can result in poor fits. The obtained parameters often require manual fine-tuning, making reproducibility of the method problematic. The CRNN addresses this issue by automatically determining the parameters that best model the experimental data using gradient descent, thus eliminating the need for manual tuning and ensuring reproducibility.

Furthermore, as noted in Table 4, the linear fit for the final stage in a four-stage model can be so poor that some parameters from stage 3 need to be used as initial guesses. Sun et al. [31] and Feng et al. [37] instead modeled the heat release of the final stage using a cumulative enthalpy method, which measures the total energy released by the last stage of the process and reuses the same function in future simulations. While this method is simple to implement, it does not generalize well to simulations outside of the ARC test because it does not attempt to model the dynamics of the stage. The CRNN method, however, is able to automatically find parameters governing the dynamics of stage 4, removing the need for approximations such as the cumulative enthalpy method.

4.3 21700 battery cell simulation

To demonstrate the fitted parameters in a realistic scenario, 3D simulations of a single 21700 cell were conducted under ARC and oven test conditions. Figure (7a) depicts the battery geometry. Thermal runaway was modeled using the modified energy equation, which includes an additional source term S_{TR} , given by

$$\rho c_p \frac{\partial T}{\partial t} = \nabla \cdot (\kappa \nabla T) + S_{TR}, \quad (19)$$

where ρ is the density, c_p is the heat capacity, and κ is the thermal conductivity. S_{TR} is then given by the fitting values obtained from the 0D model, that is

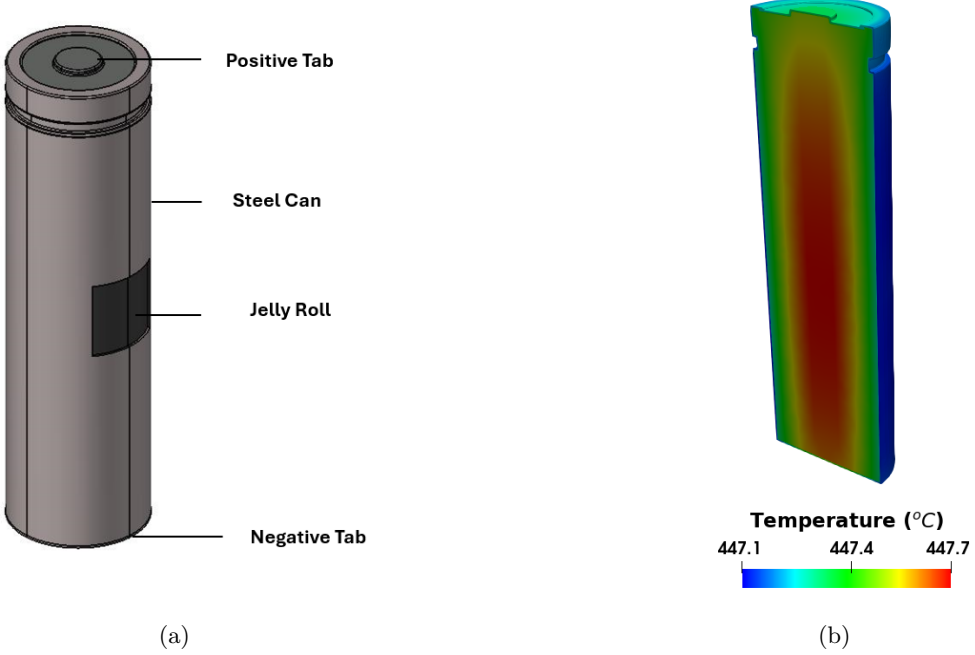


Figure 7: (a) Geometry of cell showing the can, tabs and jellyroll (b) Simulated temperature distribution during an ARC test

Component	Density (kg/m^3)	Specific Heat (J/kgK)	Conductivity (W/mK)
Jelly Roll	161	191	$(k_r, k_\theta, k_h) = (0.3, 28, 28)$
Steel Can	7917	460	14
Tabs	2770	986	175

Table 5: Properties of cell components described in Figure 7a

$$S_{TR} = \sum_{i=1}^N h_i \frac{d\alpha_i}{dt}, \quad (20)$$

Where h_i represents the enthalpy of different battery components. S_{TR} is active only within the jellyroll of the cell and is modeled using a four-stage thermal runaway model and the parameters obtained in Section 4.2. The governing energy equation includes boundary conditions for radiation and natural convection. In the ARC test, the ambient temperature is determined by the temperature recorded inside the chamber. For the oven test, the temperature reference is a single value representing the oven temperature. While more accurate simulations could incorporate natural convection volume surrounding the cell (e.g. the ARC chamber), these were simplified in the current simulations. Simulations were performed in the multi-purpose CFD software Altair® AcuSolve®. The governing Equation (19) is discretized using a Galerkin least squares stabilized finite element method. The battery geometry consisted of three main components: the jellyroll; the aluminium positive and negative tabs/terminals; and a steel can. A summary of the material properties for each of these components is provided in Table 5. The jellyroll, an effective material representation of the true wound geometry, has cylindrical anisotropic properties for thermal conductivity; the through-plane conductivity is significantly lower than in-plane conductivity.

Figure (7b) shows the temperature distribution in the cell during thermal runaway, highlighting the core of the battery heating up as the components of the jellyroll decompose. Figure (8a) displays the mean temperature history from a 3D ARC test simulation, compared to experimental temperature measurements. The model accurately predicts the occurrence and peak temperature of thermal run-

away, although some deviation afterwards was observed due to differing experimental and simulation conditions.

Oven test results in Figure (8b) for temperatures of 160°C , 200°C , and 240°C show expected trends: higher oven temperatures accelerate thermal runaway and result in higher peak temperatures. These findings demonstrate that the thermal runaway model, derived using parameters from CRNN, effectively predicts thermal behaviour in 3D simulations under varying physical and environmental conditions.

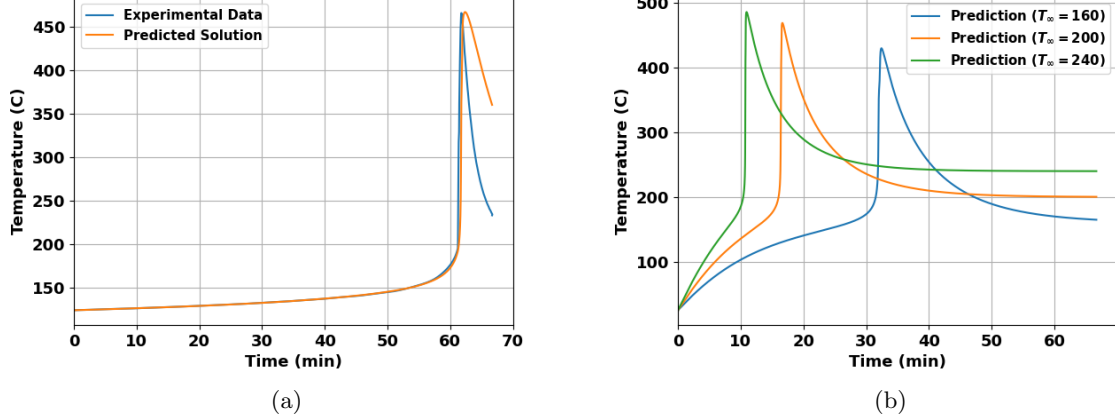


Figure 8: (a) Simulating the ARC test in 3D. (b) Simulating oven tests in 3D at various oven temperatures, observing an expected trend in temperature evolution.

5 Conclusion

This work explored using Chemical Reaction Neural Networks (CRNNs) to perform kinetic parameter fitting of multi-stage thermal runaway models governed by the Arrhenius equations to ARC data. The issues with using linearization to obtain the kinetic parameters were discussed and demonstrated, and the linear fit results were improved using a CRNN for both two-stage and four-stage models. The obtained parameters showed much better agreement with experimental data. The four-stage fit was also used to simulate ARC and oven tests in 3D, with results showing agreement with experiments. This further demonstrated the applicability of the derived thermal runaway models to simulations involving batteries or battery packs, where thermal runaway is a major safety concern and hence is a crucial design factor. The proposed method is flexible and can generalize to several stages, cell types, and stoichiometries, representing a step toward enhanced battery pack safety through simulation-driven design.

6 CRediT Authorship Statement

Saakaar Bhatnagar: Conceptualization, Formal Analysis, Methodology, Software, Visualization, Writing- Original Draft

Andrew Comerford: Conceptualization, Project Administration, Supervision, Validation, Visualization, Writing- Review and Editing

Zelu Xu: Conceptualization, Formal Analysis, Validation

Davide Berti Polato: Data Curation, Investigation, Resources

Araz Banaeizadeh: Project Administration, Supervision, Writing- Review and Editing

Alessandro Ferraris: Data Curation, Investigation, Resources

7 Funding Sources

This research received no specific grant from funding agencies in the public, commercial, or not-for-profit sectors.

References

- [1] Xuning Feng, Minggao Ouyang, Xiang Liu, Languang Lu, Yong Xia, and Xiangming He. Thermal runaway mechanism of lithium ion battery for electric vehicles: A review. *Energy storage materials*, 10:246–267, 2018.
- [2] R Spotnitz and J Franklin. Abuse behavior of high-power, lithium-ion cells. *Journal of power sources*, 113(1):81–100, 2003.
- [3] Xuning Feng, Languang Lu, Minggao Ouyang, Jiangqiu Li, and Xiangming He. A 3d thermal runaway propagation model for a large format lithium ion battery module. *Energy*, 115:194–208, 2016.
- [4] Andrey W Golubkov, David Fuchs, Julian Wagner, Helmar Wiltsche, Christoph Stangl, Gisela Fauler, Gernot Voitic, Alexander Thaler, and Viktor Hacker. Thermal-runaway experiments on consumer li-ion batteries with metal-oxide and olivin-type cathodes. *Rsc Advances*, 4(7):3633–3642, 2014.
- [5] TD Hatchard, DD MacNeil, A Basu, and JR Dahn. Thermal model of cylindrical and prismatic lithium-ion cells. *Journal of The Electrochemical Society*, 148(7):A755, 2001.
- [6] Gi-Heon Kim, Ahmad Pesaran, and Robert Spotnitz. A three-dimensional thermal abuse model for lithium-ion cells. *Journal of power sources*, 170(2):476–489, 2007.
- [7] Peng Peng and Fangming Jiang. Thermal safety of lithium-ion batteries with various cathode materials: A numerical study. *International Journal of Heat and Mass Transfer*, 103:1008–1016, 2016.
- [8] Paul T Coman, Eric C Darcy, Christian T Veje, and Ralph E White. Modelling li-ion cell thermal runaway triggered by an internal short circuit device using an efficiency factor and arrhenius formulations. *Journal of The Electrochemical Society*, 164(4):A587, 2017.
- [9] Peter J Bugryniec, Jonathan N Davidson, and Solomon F Brown. Computational modelling of thermal runaway propagation potential in lithium iron phosphate battery packs. *Energy Reports*, 6:189–197, 2020.
- [10] Depeng Kong, Gongquan Wang, Ping Ping, and Jenifer Wen. Numerical investigation of thermal runaway behavior of lithium-ion batteries with different battery materials and heating conditions. *Applied Thermal Engineering*, 189:116661, 2021.
- [11] Ashish V Shelkea, Jonathan EH Bustom, Jason Gill, Daniel Howard, Rhiannon CE Williams, Elliott Read, Ahmed Abaza, Brian Cooper, Philp Richards, and Jennifer X Wen. Combined numerical and experimental studies of 21700 lithium-ion battery thermal runaway induced by different thermal abuse. *International Journal of Heat and Mass Transfer*, 194:123099, 2022.
- [12] Ping Ping, Qingsong Wang, Youngmann Chung, and Jennifer Wen. Modelling electro-thermal response of lithium-ion batteries from normal to abuse conditions. *Applied energy*, 205:1327–1344, 2017.
- [13] Xuning Feng, Xiangming He, Minggao Ouyang, Li Wang, Languang Lu, Dongsheng Ren, and Shriram Santhanagopalan. A coupled electrochemical-thermal failure model for predicting the thermal runaway behavior of lithium-ion batteries. *Journal of The Electrochemical Society*, 165(16):A3748–A3765, 2018.

- [14] Haodong Chen, Jonathan EH Biston, Jason Gill, Daniel Howard, Rhiannon CE Williams, Elliott Read, Ahmed Abaza, Brian Cooper, and Jennifer X Wen. A simplified mathematical model for heating-induced thermal runaway of lithium-ion batteries. *Journal of The Electrochemical Society*, 168(1):010502, 2021.
- [15] MN Richard and JR Dahn. Accelerating rate calorimetry study on the thermal stability of lithium intercalated graphite in electrolyte. i. experimental. *Journal of The Electrochemical Society*, 146 (6):2068, 1999.
- [16] Hang Wu, Siqi Chen, Jie Chen, Changyong Jin, Chengshan Xu, Xinyu Rui, Hungjen Hsu, Yuejiu Zheng, and Xuning Feng. Dimensionless normalized concentration based thermal-electric regression model for the thermal runaway of lithium-ion batteries. *Journal of Power Sources*, 521: 230958, 2022.
- [17] Boxia Lei, Wenjiao Zhao, Carlos Ziebert, Nils Uhlmann, Magnus Rohde, and Hans Jürgen Seifert. Experimental analysis of thermal runaway in 18650 cylindrical li-ion cells using an accelerating rate calorimeter. *Batteries*, 3(2):14, 2017.
- [18] William Q Walker, Kylie Cooper, Peter Hughes, Ian Doemling, Mina Akhnoukh, Sydney Taylor, Jacob Darst, Julia Billman, Matthew Sharp, David Petrushenko, et al. The effect of cell geometry and trigger method on the risks associated with thermal runaway of lithium-ion batteries. *Journal of Power Sources*, 524:230645, 2022.
- [19] Dongsheng Ren, Xiang Liu, Xuning Feng, Languang Lu, Minggao Ouyang, Jianqiu Li, and Xiangming He. Model-based thermal runaway prediction of lithium-ion batteries from kinetics analysis of cell components. *Applied energy*, 228:633–644, 2018.
- [20] Yu Wang, Dongsheng Ren, Xuning Feng, Li Wang, and Minggao Ouyang. Thermal kinetics comparison of delithiated li $[nixcoymn1-xy] o_2$ cathodes. *Journal of Power Sources*, 514:230582, 2021.
- [21] Gongquan Wang, Ping Ping, Depeng Kong, Rongqi Peng, Xu He, Yue Zhang, Xinyi Dai, and Jennifer Wen. Advances and challenges in thermal runaway modelling of lithium-ion batteries. *The Innovation*, 2024.
- [22] Benjamin C Koenig, Peng Zhao, and Sili Deng. Accommodating physical reaction schemes in dsc cathode thermal stability analysis using chemical reaction neural networks. *Journal of Power Sources*, 581:233443, 2023.
- [23] Weiqi Ji and Sili Deng. Autonomous discovery of unknown reaction pathways from data by chemical reaction neural network. *The Journal of Physical Chemistry A*, 125(4):1082–1092, 2021.
- [24] Ricky TQ Chen, Yulia Rubanova, Jesse Bettencourt, and David K Duvenaud. Neural ordinary differential equations. *Advances in neural information processing systems*, 31, 2018.
- [25] Anjana Puliyanda, Karthik Srinivasan, Zukui Li, and Vinay Prasad. Benchmarking chemical neural ordinary differential equations to obtain reaction network-constrained kinetic models from spectroscopic data. *Engineering Applications of Artificial Intelligence*, 125:106690, 2023.
- [26] Tim Kircher, Felix A Döppel, and Martin Votsmeier. Global reaction neural networks with embedded stoichiometry and thermodynamics for learning kinetics from reactor data. *Chemical Engineering Journal*, page 149863, 2024.
- [27] Homer E Kissinger et al. Variation of peak temperature with heating rate in differential thermal analysis. *Journal of research of the National Bureau of Standards*, 57(4):217–221, 1956.
- [28] Michael E Brown. The prout-tompkins rate equation in solid-state kinetics. *Thermochimica acta*, 300(1-2):93–106, 1997.
- [29] Mathilde Grandjacques, Pierre Kuntz, Philippe Azaïs, Sylvie Genies, and Olivier Raccourt. Thermal runaway modelling of li-ion cells at various states of ageing with a semi-empirical model based on a kinetic equation. *Batteries*, 7(4):68, 2021.

- [30] Shin-Chih Chen, Yung-Yun Wang, and Chi-Chao Wan. Thermal analysis of spirally wound lithium batteries. *Journal of the Electrochemical Society*, 153(4):A637, 2006.
- [31] Tao Sun, Luyan Wang, Dongsheng Ren, Zhihe Shi, Jie Chen, Yuejiu Zheng, Xuning Feng, Xuebing Han, Languang Lu, Li Wang, et al. Thermal runaway characteristics and modeling of lifepo4 power battery for electric vehicles. *Automotive Innovation*, 6(3):414–424, 2023.
- [32] Atilim Gunes Baydin, Barak A Pearlmutter, Alexey Andreyevich Radul, and Jeffrey Mark Siskind. Automatic differentiation in machine learning: a survey. *Journal of machine learning research*, 18(153):1–43, 2018.
- [33] James Bradbury, Roy Frostig, Peter Hawkins, Matthew James Johnson, Chris Leary, Dougal Maclaurin, George Necula, Adam Paszke, Jake VanderPlas, Skye Wanderman-Milne, and Qiao Zhang. JAX: composable transformations of Python+NumPy programs, 2018. URL <http://github.com/google/jax>.
- [34] Patrick Kidger. *On Neural Differential Equations*. PhD thesis, University of Oxford, 2021.
- [35] Anne Kværnø. Singly diagonally implicit runge–kutta methods with an explicit first stage. *BIT Numerical Mathematics*, 44(3):489–502, 2004.
- [36] Diederik P Kingma and Jimmy Ba. Adam: A method for stochastic optimization. *arXiv preprint arXiv:1412.6980*, 2014.
- [37] Xuning Feng, Xiangming He, Minggao Ouyang, Li Wang, Languang Lu, Dongsheng Ren, and Shriram Santhanagopalan. A coupled electrochemical-thermal failure model for predicting the thermal runaway behavior of lithium-ion batteries. *Journal of The Electrochemical Society*, 165(16):A3748–A3765, 2018.